



## Corner states of topological fullerenes

Andreas Rüegg,<sup>1,2</sup> Sinisa Coh,<sup>1,3</sup> and Joel E. Moore<sup>1,3</sup>

<sup>1</sup>*Department of Physics, University of California, Berkeley, Berkeley, California 94720, USA*

<sup>2</sup>*Theoretische Physik, ETH Zürich, CH-8093 Zürich, Switzerland*

<sup>3</sup>*Materials Science Division, Lawrence Berkeley National Laboratory, Berkeley, California 94720, USA*

(Received 15 August 2013; published 21 October 2013)

The unusual electronic properties of the quantum spin Hall or Chern insulator become manifest in the form of robust edge states when samples with boundaries are studied. In this work, we ask if and how the topologically nontrivial electronic structure of these two-dimensional systems can be passed on to their zero-dimensional relatives, namely, fullerenes or other closed-cage molecules. To address this question, we study Haldane's honeycomb lattice model on polyhedral nanosurfaces. We find that for sufficiently large surfaces, characteristic corner states appear for parameters for which the planar model displays a quantized Hall effect. In the electronic structure, these corner states show up as in-gap modes which are well separated from the quasicontinuum of states. We discuss the role of finite-size effects and how the coupling between the corner states lifts the degeneracy in a characteristic way determined by the combined Berry phases which leads to an effective magnetic monopole of charge 2 at the center of the nanosurface. Experimental implications for fullerenes in the large spin-orbit regime are also pointed out.

DOI: [10.1103/PhysRevB.88.155127](https://doi.org/10.1103/PhysRevB.88.155127)

PACS number(s): 71.20.Tx, 71.55.-i, 71.20.Ps, 73.43.-f

### I. INTRODUCTION

The nontrivial topological electronic properties of two-dimensional Chern insulators<sup>1,2</sup> (quantum anomalous Hall insulators) or quantum spin Hall insulators<sup>3-7</sup> imply the existence of topologically protected boundary modes in systems with boundaries. While the chiral edge states of the Chern insulator are immune to backscattering and hence robust against all forms of weak disorder,<sup>8</sup> the helical edge states of a quantum spin Hall insulator are at least protected against elastic scattering off nonmagnetic impurities until the edge electron-electron interactions are rather strong.<sup>9,10</sup> In both cases, unless disorder is so strong as to drive a phase transition, edge states are present independent of the shape or microscopic structure of the boundary. Because these boundary modes live in the bulk gap of the single-particle spectrum, they appear as in-gap levels in the total density of states [see Fig. 1(a)]. This provides a way to distinguish a topological from a trivial insulator for which edge states are generically absent, and the spectrum remains gapped in the presence of a boundary. On the other hand, if we use periodic instead of open boundary conditions [i.e., consider the system on a torus, Fig. 1(b)], edge states are gapped out. In this case, the spectrum of a topological insulator is indistinguishable from the spectrum of a trivial insulator. One might expect that this conclusion remains valid if the system is put on any closed (meaning, without boundary) surface.

In this paper, by studying Haldane's honeycomb lattice model<sup>1</sup> on topologically *spherical* nanosurfaces (i.e., polyhedra), we provide counterexamples to this naive expectation. Namely, we demonstrate that on such closed but sufficiently large surfaces, the nontrivial topological invariant of the two-dimensional model is revealed in the electronic spectrum: choosing parameters for which the planar system has a nonvanishing Chern number  $C = \pm 1$ , we identify characteristic in-gap states which are well separated from the quasicontinuum of the remaining levels. Moreover, we find that these in-gap levels correspond to eigenstates which are

localized at the *corners* of the polyhedral surfaces. In analogy with the closed-cage molecules formed from carbon atoms,<sup>11</sup> we dub the systems displaying the characteristic corner states as *topological fullerenes*. A summary of our main results is illustrated in Fig. 1. To avoid confusion, we stress that our nomenclature does *not* refer to a topological invariant of a zero-dimensional free-fermion system.<sup>12,13</sup> [An example of such a zero-dimensional invariant was given by Kitaev:<sup>12</sup> in the absence of time-reversal symmetry (class A), the number of occupied states below the Fermi energy determines a  $\mathbb{Z}$  index.] Instead, we ask the question of what happens to a two-dimensional topologically nontrivial system if it is put on a closed two-dimensional nanosurface. Hence, the name “topological fullerenes” solely refers to the topologically nontrivial properties of the two-dimensional parent system.

In passing, we note that closed (spherical) surfaces with quantized Hall conductivity similar to the ones studied in this paper also appear when the orbital magnetoelectric effect is analyzed via the theory of electrical polarization:<sup>14</sup> for a three-dimensional (3D) solid, the orbital-electronic contribution to the magnetoelectric coupling has a quantum of indeterminacy. This quantum corresponds to the possibility of absorbing layers with quantized Hall conductivity on the surfaces of the solid.

Our theoretical analysis focuses on the tetrahedral, octahedral, and icosahedral nanosurfaces. These polyhedral surfaces can be constructed from the planar honeycomb lattice by cutting out appropriate wedges and gluing the edges back together.<sup>15</sup> While spherical carbon fullerenes,<sup>11,16</sup> such as the  $C_{60}$  buckyball, have the shape of an icosahedron, materials like boron nitride<sup>17</sup> or transition-metal dichalcogenides<sup>18,19</sup> prefer to form octahedral fullerenes. We are not aware of a material which realizes a tetrahedral nanosurface, but from a theoretical perspective it is instructive (and simple enough) to include this surface in our discussion as well.

To date, we do not know of an experimental system realizing Haldane's honeycomb lattice model. However, there are

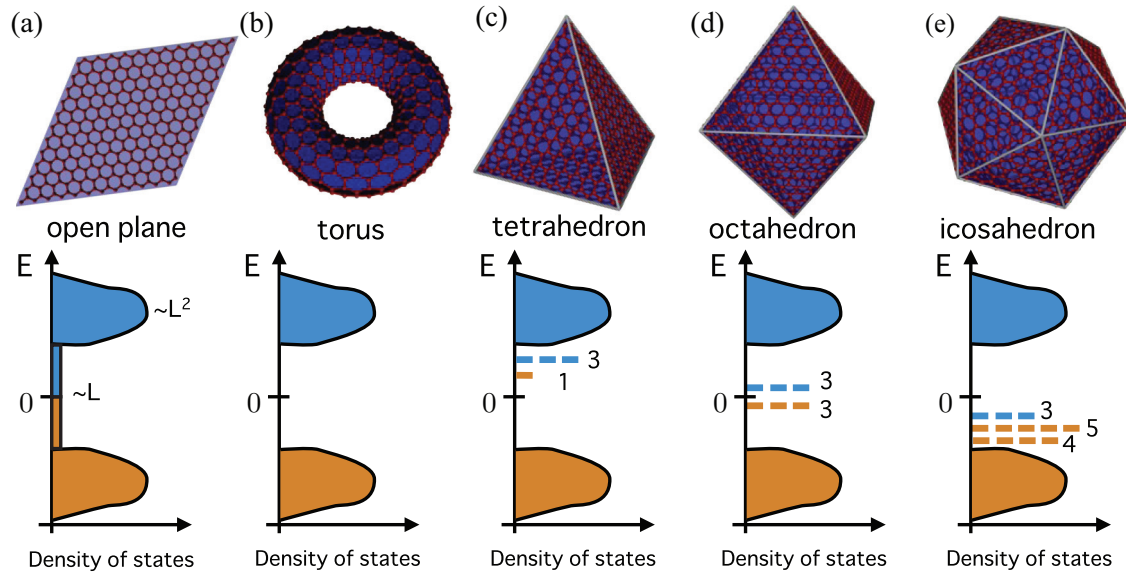


FIG. 1. (Color online) Schematics of the electronic spectrum of the Haldane model in the Chern-insulator phase on various geometries. (a) For a finite open system, edge states appear in the gap. The number of in-gap states is proportional to the circumference  $L$  of the sample while the number of states in the valence or conduction bands is proportional to  $L^2$ . (b) If periodic boundary conditions are employed to form a torus, the spectrum is gapped as for the infinite planar model. If the Haldane model is studied on polyhedral surfaces (c), (d), and (e), a finite number of in-gap states is observed. The number of in-gap states depends on the geometry of the nanosurface, namely, the number of corners. Moreover, the degeneracy of the in-gap levels is lifted in a characteristic way as indicated. In the bottom panels, occupied states are colored orange, while empty states are in blue.

interesting proposals that a time-reversal-invariant quantum spin Hall insulator with nontrivial  $\mathbb{Z}_2$  index can be realized on the honeycomb lattice.<sup>3,4</sup> The first route to stabilizing such a phase considers the possibility of inducing a large spin-orbit coupling in graphene via heavy adatoms.<sup>20,21</sup> The second approach seeks for alternative graphenelike materials with large intrinsic spin-orbit coupling, such as a single Bi bilayer,<sup>22</sup> silicene (2D Si),<sup>23</sup> or 2D tin.<sup>24</sup> There are first experimental indications for the existence of a topological insulator phase in Bi bilayers<sup>25</sup> and it is reasonable to assume that if the two-dimensional (2D) versions exist, also closed-cage molecules might be synthesized, eventually.

The remainder of the paper is organized as follows: In Sec. II, we relate the corners of the polyhedral surfaces to topological lattice defects called *disclinations* and we specify how to define Haldane's model on the considered nanosurfaces. In Sec. III, we briefly review the properties of an isolated disclination in the Haldane model and provide a topological perspective on the existence of nontrivial bound states. In Sec. IV, we present results from numerically diagonalizing various polyhedral systems to demonstrate the existence of the corner states. We also discuss the finite-size effects which should be small in order to identify the in-gap states. In Sec. V, we investigate how the degeneracy of the in-gap levels is lifted due to the coupling between the corner states in a finite system. To recover the observed splitting, we include Berry phase terms which can be represented as an effective magnetic monopole of charge 2 at the center of the polyhedral surfaces. We conclude in Sec. VI by summarizing our results and providing a more detailed discussion of possible experimental systems.

## II. MODEL FOR TOPOLOGICAL FULLERENES

### A. Polyhedral nanosurfaces

To study topological effects on closed-cage molecules, we first generalize Haldane's Chern-insulator model on the honeycomb lattice to polyhedral nanosurfaces. It is well known that a polyhedral nanosurface can not be formed using only hexagons.<sup>11</sup> Instead,  $n$ -gons with  $n < 6$  have to be introduced, and in the following we briefly discuss the general structure of such molecules. The fundamental relation satisfied by all the closed nanosurfaces is given by Euler's famous formula

$$V - E + F = \chi. \quad (1)$$

Equation (1) relates the number of faces  $F$ , the number of vertices  $V$ , and the number of edges  $E$  to the Euler characteristic  $\chi$ . For a spherical polyhedral surface,  $\chi = 2$  while for the torus  $\chi = 0$ . For a given  $n < 6$ , one can now easily compute the number  $N$  of  $n$ -gons which are required in addition to the number  $H$  of hexagons to form a closed surface, by noting that

$$F = N + H, \quad 2E = nN + 6H, \quad 3V = nN + 6H.$$

In combination with Eq. (1),  $N$  can be obtained as

$$N = \frac{\chi}{1 - n/6} = \frac{6\chi}{f}, \quad (2)$$

where  $f = 6 - n$ . [Note that  $H$  is undetermined by Eq. (1).] For the torus ( $\chi = 0$ ), it follows that  $N = 0$  and no defects are necessary.<sup>26</sup> On the other hand, for the polyhedral surfaces ( $\chi = 2$ ),  $N$  is nonvanishing. Specifically, an icosahedral surface can be formed with additional 12 pentagons ( $f = 1$ ),

an octahedral surface with additional 6 squares ( $f = 2$ ), or a tetrahedral surface with additional 4 triangles ( $f = 3$ ). In essence, the total curvature needed to form a spherelike molecule with  $\chi = 2$  is concentrated at the  $n$ -gons with  $n < 6$ . Hence, the  $n$ -gonal lattice defects form the corners of the polyhedra and, as discussed in the following, are crucial for understanding the electronic structure of the Haldane model defined on these nanosurfaces.

### B. Tight-binding model

We are now in a position to define the Haldane model on the polyhedral surfaces discussed above. The tight-binding model is given by<sup>1</sup>

$$\begin{aligned} \mathcal{H} = & -t \sum_{\langle i,j \rangle} (c_i^\dagger c_j + \text{H.c.}) \\ & - t_2 \sum_{\langle\langle i,j \rangle\rangle} (e^{-i\phi_{ij}} c_i^\dagger c_j + \text{H.c.}) + \mathcal{H}_\Delta. \end{aligned} \quad (3)$$

Here,  $c_i^\dagger$  and  $c_i$  are fermionic creation and annihilation operators of spinless electrons on site  $i$ , respectively. The nearest-neighbor hopping amplitude is  $t = 1$  which sets the unit of energy and  $t_2$  is the second-neighbor hopping with phase factors  $e^{i\phi_{ij}}$ . In the planar model, the phases  $\phi_{ij}$  are chosen such that a staggered flux configuration, which preserves both the original unit cell and the sixfold rotation symmetry, is realized.<sup>1</sup> For the studied nanosurfaces, we use the bulk assignment of  $\phi_{ij}$  for all the hexagons. Indeed, it is possible to choose the handedness of  $\phi_{ij}$  consistently on all the faces and across the edges where they meet. Using the concept of a local Chern vector as introduced recently in Ref. 27, this choice guarantees a local Chern vector which always points either outward or inward of the surface. For the most part, we will set  $\phi_{ij} = \pm\pi/2$  such that the second-neighbor hopping is purely imaginary. Across the  $n$ -gons with  $n = 3, 4$ , or  $5$ , the phase factors are not uniquely defined and we therefore choose  $t_2 = 0$ . However, the results to be derived do not depend in an important way on the choice of the second-neighbor hopping across the  $n$ -gons, as they can be obtained from general analytical arguments that are independent of this choice.

The last term  $\mathcal{H}_\Delta$  in Eq. (3) is identical to zero for the tetrahedral and icosahedral nanosurfaces  $\mathcal{H}_\Delta = 0$ . For the octahedral surfaces, on the other hand, it is defined as

$$\mathcal{H}_\Delta = \Delta \left( \sum_{i \in A} n_i - \sum_{i \in B} n_i \right), \quad (4)$$

where  $n_i = c_i^\dagger c_i$  and  $A$  and  $B$  refer to the two sublattices. The staggered sublattice potential  $\mathcal{H}_\Delta$  can stabilize a topologically trivial phase in the planar system.<sup>1</sup> The definition (4) requires a *global* assignment of two sublattices  $A$  and  $B$ . We therefore include the staggered sublattice potential only on the octahedral surfaces. Both tetrahedral and icosahedral surfaces do not allow for a global definition of two sublattices, and attempting to define Eq. (4) would require us to introduce domain walls across which the definition of the  $A$ - $B$  sublattices changes.

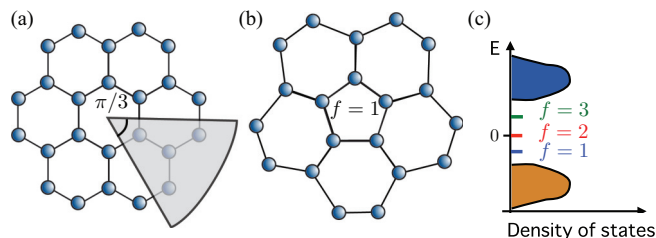


FIG. 2. (Color online) (a) An isolated wedge disclination is constructed by cutting out  $f$  times a  $\pi/3$  wedge and gluing the two sides back together. (b) For  $f = 1$ , the disclination core is formed by a pentagon. (c) In the Haldane model, different types of disclinations induce in-gap states with different energies.

## III. ISOLATED DISCLINATION

### A. Overview of results

The  $n$ -gonal lattice defects appearing at the corners of the polyhedral surfaces are known as wedge disclinations<sup>28</sup> and are characterized by the *Frank index*  $f = 6 - n$ . Disclinations are topological defects of the rotational order and have been subject to intense studies in the context of graphene and fullerenes.<sup>15,29–31</sup> In the cut-and-glue construction, the integer  $f > 0$  ( $f < 0$ ) has the meaning of counting the number of removed (added)  $\pi/3$  wedges [see Figs. 2(a) and 2(b)]. Note that for  $f > 0$ , an isolated disclination forms the tip of a nanocone.<sup>32</sup>

The properties of an isolated disclination in the topological phase of the Haldane model have recently been studied theoretically.<sup>33</sup> The main observation was that an isolated defect in the Chern-insulator phase with Chern number  $C$  acts as a source of a fictitious flux

$$\phi_f = \text{sign}(C) \frac{f}{4} \phi_0 \pmod{\phi_0}, \quad (5)$$

which pierces the defect core, where  $\phi_0 = h/e$  is the quantum of flux. The quantized Hall conductivity  $\sigma_{xy} = Ce^2/h$  implies that an isolated defect binds a fractional charge given by

$$q_f = \sigma_{xy} \phi_f = e|C| \frac{f}{4} \pmod{e}. \quad (6)$$

The defect states show up as single in-gap levels in the local density of states with an energy which increases for increasing  $f > 0$  [see Fig. 2(c)]. It has been argued<sup>33</sup> that measuring such defect states would provide an alternative probe of the topological phase, in analogy with dislocation modes in weak or crystalline topological insulators.<sup>34–37</sup>

Finally, let us clarify in which sense we use the expression “fractional charges.” We first recap that the subject of this paper is a noninteracting model on interesting but static lattice geometries. Therefore, unlike quasiparticle excitations of fractional quantum Hall liquids, the fractional charges in our system are not emergent dynamical excitations. Rather, they are bound to topological defects in a classical field (describing the lattice), which couples to the fermion system. In this respect, the fractional charges we observe at disclinations are more closely related to Majorana modes in vortices of topological superconductors<sup>38</sup> or the quantum number fractionalization at domain walls in polyacetylene.<sup>39</sup> Similar to the aforementioned examples, we find that the quantum

mechanical wave function associated with the fractional charge is exponentially localized at the defect for an infinite system, justifying the used terminology. We mention also that in-gap states localized at point defects on the hexagonal lattice have previously been studied in other contexts.<sup>40–42</sup> Furthermore, disclinations also attracted attention in two-dimensional crystalline topological superconductors where Majorana bound states can be realized.<sup>43,44</sup>

### B. Implications from particle-hole symmetry

In the presence of discrete symmetries,<sup>12,45</sup> a topological classification of topological defects exists.<sup>46</sup> Here, we focus on the role of particle-hole symmetry (class D) which gives rise to a  $\mathbb{Z}_2$  classification of point defects in two dimensions. The  $\mathbb{Z}_2$  index signals the presence or absence of a single  $E = 0$  bound state. In the case of a superconductor, the  $E = 0$  mode corresponds to a Majorana bound state, while in a spin-polarized insulator, the nontrivial defect binds a fractional charge  $e/2$ . As long as the particle-hole symmetry is preserved, a trivial defect can not be deformed into a nontrivial defect without closing of the bulk gap. As we discuss in the following, the bound states of disclinations in the Haldane model can be understood from this perspective.

We first discuss the condition for particle-hole symmetry in the Haldane model which implies a specific form of the (first quantized) Hamiltonian matrix  $\hat{h}$ . We write  $\hat{h}$  in a sublattice basis as

$$\hat{h} = \begin{pmatrix} \hat{h}_{AA} & \hat{h}_{AB} \\ \hat{h}_{AB}^\dagger & \hat{h}_{BB} \end{pmatrix} \quad (7)$$

and denote the eigenfunction of  $\hat{h}$  with energy  $E$  as  $\psi(j)$ :

$$\sum_j \hat{h}_{ij} \psi(j) = E \psi(i). \quad (8)$$

A particle-hole-symmetric spectrum is guaranteed if the particle-hole conjugate wave function  $\varphi(i) = \sigma_z \psi(i)^*$  is an eigenstate of  $\hat{h}$  with energy  $-E$ :

$$\sum_j \hat{h}_{ij} \varphi(j) = -E \varphi(i). \quad (9)$$

Here,  $\sigma_z$  is the third Pauli matrix acting on the sublattice degree of freedom ( $A$ - $B$ ). Equation (9) implies that

$$\sigma_z \hat{h}^* \sigma_z = -\hat{h} \quad (10)$$

or, using Eq. (7),

$$\hat{h}_{AB}^* = \hat{h}_{AB}, \quad \hat{h}_{AA}^* = -\hat{h}_{AA}, \quad \hat{h}_{BB}^* = -\hat{h}_{BB}. \quad (11)$$

In other words, a particle-hole-symmetric spectrum is guaranteed if the hopping between  $A$  and  $B$  sublattices is real but purely imaginary among either  $A$  or  $B$  sites.<sup>47</sup> Notice that the particle-hole symmetry in the Haldane model relies on the bipartiteness of the honeycomb lattice. Therefore, despite the formal analogy, it is physically very distinct from the built-in particle-hole symmetry of a superconductor in the Bogoliubov–de Gennes description. In particular, lattice defects in the Haldane model have the potential to violate the symmetry. In the following, we discuss how this fact can be used to deduce certain properties of an isolated disclination.

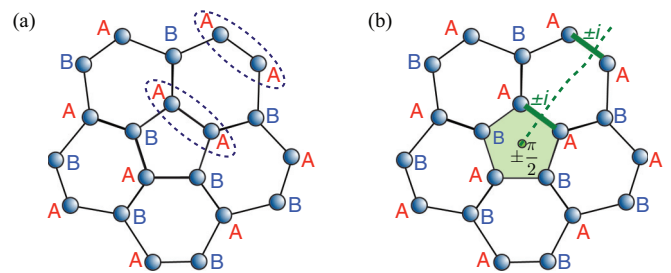


FIG. 3. (Color online) (a) The  $f = 1$  disclination violates the particle-hole symmetry of the Haldane model with purely imaginary second-neighbor hopping because two  $A$  sites meet across the seam. (b) Particle-hole symmetry can be restored by piercing the defect core with an external flux  $\phi_e = \pm\phi_f/4$ .

For a disclination with odd  $f$ , the particle-hole symmetry is violated. This is easy to understand because two  $A$  sites (or two  $B$  sites) meet across the seam, as illustrated in Fig. 3(a) for the case  $f = 1$ . Hence, the conditions (11) are violated. However, one can restore the particle-hole symmetry by piercing the center of the defect with an external flux  $\phi_e = \pm\phi_0/4$ : if we bring the Dirac string into line with the seam, as shown in Fig. 3(b), then all the bonds crossing the Dirac string acquire an additional phase factor  $\pm i$ . In particular, the nearest-neighbor hopping between two  $A$  sites across the seam becomes purely imaginary. Similarly, the second-neighbor hopping between  $A$  and  $B$  sites across the seam becomes real. Thus, with an external flux  $\phi_e = \pm\phi_0/4$ , the conditions (11) are fulfilled and the spectrum is particle-hole symmetric again. As a consequence, we know that the charge bound to the defect is either 0 or  $e/2 \bmod e$ :

$$q = q_f \pm \frac{eC}{4} = 0 \text{ or } e/2 \bmod e, \quad (12)$$

where  $q_f$  is the intrinsic defect charge and  $\pm eC/4$  is the charge induced by the external flux. If in addition  $C$  is odd, we immediately conclude that  $q_f = \pm e/4$ . Hence, there is always a nontrivial bound state. Using the linearity in  $f$ , we find that the bound charge for a general  $f$  is  $q_f = \pm f e/4 \bmod e$ . Thus, for odd  $C$ , there is a  $\mathbb{Z}_4$  classification of disclination defects. For even  $C$ , Eq. (12) does not provide additional information.

From the discussion above, it is clear that the disclination bound states are independent of a specific model as long as the particle-hole symmetry is realized via the conditions (11). It then follows that for even  $f$  the particle-hole symmetry is preserved and the bound state (if present) is protected against any local perturbation which preserves the conditions (11). Similarly, if  $f$  is odd, the bound state (if present) is protected against local perturbations which respect Eq. (11) in the presence of an external flux  $\phi_e = \pm\phi_0/4$ . Hence, particle-hole symmetry allows for a sharp topological distinction of the defect states.

One may object that particle-hole symmetry in electronic systems is a fine-tuned symmetry. In the Haldane model, it is, for example, easily broken if the phases  $\phi_{ij}$  of the second-neighbor hopping are tuned away from  $\pm\pi/2$ . Fortunately, direct diagonalization of the tight-binding problem in the presence of particle-hole symmetry-breaking terms indicates that Eqs. (5) and (6) still hold.<sup>33</sup> This suggests that the

results are valid beyond the particle-hole-symmetric limit. Note, however, that in order to consistently define an electronic model with an invisible seam in the presence of a disclination, it has to respect (at least on average) the  $C_3$  symmetry for even- $f$  and the  $C_6$  symmetry for odd- $f$  disclinations. The bound states are therefore only protected in the presence of these crystalline symmetries and it is an interesting open problem to show if the presence or absence of bound states can be related to appropriate rotation eigenvalues.<sup>43,48,49</sup> In the Appendix, we provide such a connection on the basis of the continuum description.

## IV. NUMERICAL RESULTS

### A. General considerations

We now return to the study of the spherical nanosurfaces and in the following, we present the results obtained from numerically diagonalizing Eq. (3) on various geometries. Because of the finite size of the molecules, there are two important differences to the case of an isolated disclination discussed in Sec. III. First, apart from the energy scale of the bulk gap  $E_g \sim |t_2|$ , the finite-size effect introduces an additional scale given by the mean-level spacing  $E_R \sim t/N_s$  where  $N_s$  denotes the number of sites. We expect that only in the regime  $E_g \gg E_R$  it is possible to spot putative in-gap states which are well separated from states of the quasicontinuum. Second, there is always an even number of corner states and they generically couple to each other, allowing in principle to push the in-gap states into the quasicontinuum. In the regime  $E_g \gg E_R$ , the coupling is expected to be weak and in-gap states are well defined.

Section IV B demonstrates that one can indeed identify in-gap states for sufficiently large systems, consistent with the analysis of isolated defects. By increasing the staggered sublattice potential in the octahedral system, we also demonstrate that the in-gap states are lost if the planar parent system is tuned into the trivial insulator with  $C = 0$ . In Sec. IV C, we discuss the finite-size effects. We therefore consider how the limit  $E_g \gg E_R$  is approached by tuning either the bulk gap via  $|t_2|$  or the mean-level spacing via the system size  $N_s$ .

### B. Corner states

Figure 4 shows the spectrum for the tetrahedron, the octahedron, and the icosahedron models with parameters  $|t_2| = 0.2$ ,  $\phi = \pi/2$ , and  $\Delta = 0$ . For these parameters, the bulk system realizes a Chern insulator with Chern number  $C = \pm 1$ . The nanosurfaces considered in Fig. 4 have  $N_s = 100, 200$ , and 500 atoms for the tetrahedron, octahedron, and icosahedron, respectively. This choice guarantees that the distance between the corners is roughly the same for the different geometries. For all the systems, the condition  $E_R \ll E_g$  is fulfilled. Indeed, one can identify a quasicontinuum of states separated by a gap. In addition, each spectrum features a characteristic number of in-gap states (some of which are degenerate, as shown in the inset):  $1 + 3 = 4$  for the tetrahedron,  $3 + 3 = 6$  for the octahedron, and  $3 + 5 + 4 = 12$  for the icosahedron. While the observed splitting of the in-gap level is always the same and will be discussed later in Sec. V, the order of the levels depends on details such as system size or the ratio  $t_2/t$ .

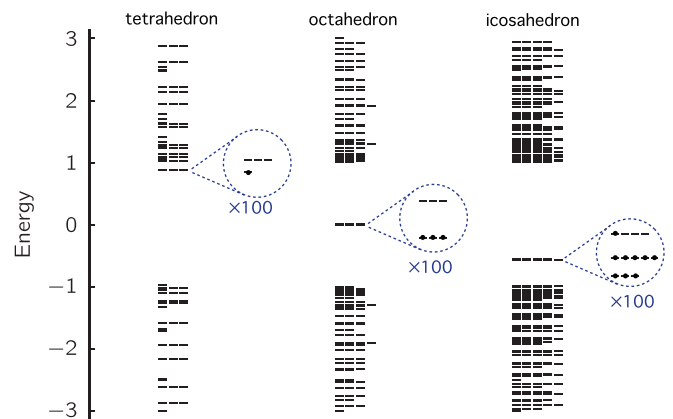


FIG. 4. (Color online) Energy levels of tetrahedron, octahedron, and icosahedron models. Corner states are clearly visible in the gap and are separated from the remaining states. The inset shows a zoom-in (by a factor 100) of the in-gap states displaying the characteristic degeneracies  $1 + 3$  for tetrahedron,  $3 + 3$  for the octahedron, and  $3 + 5 + 4$  for the icosahedron. In-gap levels which are occupied at half filling are marked with a dot. Parameters of the model (3) are  $t = 1.0$ ,  $|t_2| = 0.2$ , and  $\phi = \pi/2$ .

For the given parameters, the spectrum of the octahedron model is particle-hole symmetric as expected from the discussion in Sec. III B. On the other hand, particle-hole symmetry is violated for the tetrahedron and icosahedron models. The fractional charge bound to an isolated disclination can also be understood from the spectra in Fig. 4 when considering the half-filled systems for which the average charge per site is  $e/2$ . For the tetrahedron, one out of four in-gap states is filled. By symmetry, the wave function of this in-gap state has equal weight on each of the four corners. Therefore, it contributes an average charge  $e/4$  per corner. In the half-filled system, this charge has to compensate the fractional charge of the corner and we conclude that each defect carries a charge  $-e/4$ . Similarly, for the octahedron, three out of six states are filled, resulting in a charge  $-e/2$  per defect. Finally, for the icosahedron, 9 out of 12 levels are occupied resulting in  $-3e/4$  per defect. These values are in agreement with Eq. (6) obtained from the analysis of an isolated disclination.

The presence of nontrivial corner states is tied to the existence of a nontrivial Chern number in the corresponding bulk system. This can easily be tested by adding a staggered sublattice potential Eq. (4) which in bulk drives a transition to a gapped phase with  $C = 0$ . The corresponding result for an octahedral nanosurface is shown in Fig. 5. As a function of the sublattice potential  $\Delta$ , the spectrum changes considerably. However, as opposed to the bulk system, finite-size effects prohibit a sharp closing of a gap between the small- and large- $\Delta$  limits. Instead, a crossover at  $\Delta \approx 1$  is seen. Nevertheless, the small- and large- $\Delta$  regimes are clearly distinct by the presence or absence of the corner states. Note that a similar analysis for tetrahedral or icosahedral surfaces is not possible because in an attempt to define a staggered sublattice potential for these systems, the definition of  $A$  and  $B$  sites needs to be interchanged when crossing domain walls connecting two defects. These domain walls can act as one-dimensional

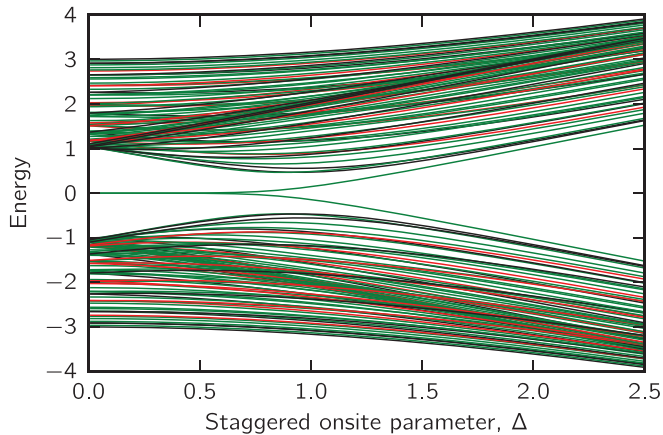


FIG. 5. (Color online) The staggered sublattice potential  $\Delta$  on the octahedral nanosurface tunes a crossover between the topological (small- $\Delta$ ) and trivial (large- $\Delta$ ) regimes. Parameters of the model (3) with  $N_s = 392$  sites are  $t = 1.0$ ,  $|t_2| = 0.2$ , and  $\phi = \pi/2$ . Nondegenerate levels are colored black, twofold-degenerate states red, threefold-degenerate states green, and fourfold-degenerate states blue.

channels introducing additional in-gap states in the large- $\Delta$  regime.<sup>50,51</sup>

### C. Finite-size effects

The notion of in-gap states requires that  $E_R \ll E_g$ . If this condition is not fulfilled, the corner states are no longer clearly separated from the rest of the spectrum and a distinction between topological and trivial regimes (as demonstrated in Fig. 5) is in general not possible. Despite this expectation, we find that the finite-size effects on the octahedral nanosurfaces have little consequences on the corner states making them well defined even if  $E_R \sim E_g$ . On the other hand, the corner states of the tetrahedral and icosahedral surfaces are more sensitive and indeed require  $E_R \ll E_g$ .

#### 1. Octahedral nanosurfaces

We start with the octahedral nanosurface. The spectrum as function of  $|t_2|$  for  $N_s = 200$  is shown in Fig. 6. Note that for the bulk system,  $t_2 = 0$  corresponds to the gapless case while a gap opens for nonzero  $|t_2|$ . On the other hand, the spectrum of the octahedral nanosurface is discrete for any  $t_2$ . Interestingly, the clearly separated corner states emerge out of a pair of triplets near  $E = 0$  for small  $t_2$  which already exists for  $t_2 = 0$ . In this limit, these states are expected to be algebraically localized at the corners<sup>29,30</sup> while for increasing  $|t_2|$  the localization length decreases, making the corner states increasingly better defined.

A similar trend is also observed for increasing system sizes at fixed  $|t_2| = 0.2$  (see Fig. 7). The spectrum was obtained for  $N_s = 32, 72, 128$ , and 200 sites. For the larger systems with  $N_s \geq 72$ , corner states which are well separated from the quasicontinuum are clearly visible. However, the characteristic pair of triplets already exists for the smallest considered system with  $N_s = 36$  sites.

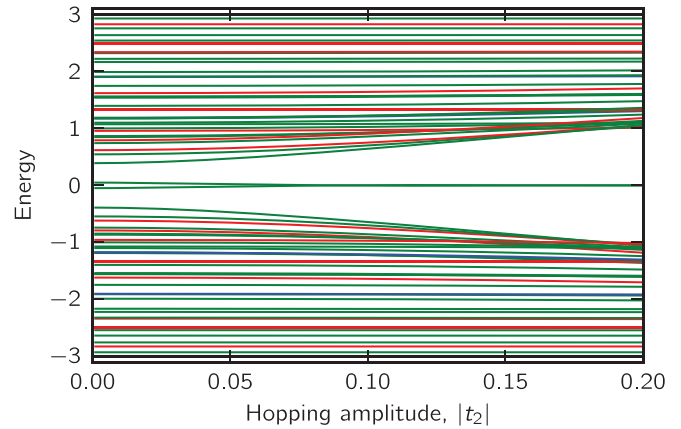


FIG. 6. (Color online) Eigenvalues of the octahedron model as a function of the second-neighbor hopping parameter amplitude  $|t_2|$ . Two threefold-degenerate corner states occur in the gap and are clearly separated from other states when  $|t_2|$  is about 0.05–0.1. Phase of the second-neighbor hopping parameter is  $\phi = \pi/2$ , the first-neighbor hopping parameter equals 1.0, and  $N_s = 200$ . Nondegenerate levels are colored black, twofold-degenerate states red, threefold-degenerate states green, and fourfold-degenerate states blue.

#### 2. Icosahedral nanosurfaces

We now turn to the icosahedral nanosurface. Figure 8 shows the spectrum as function of the second-neighbor hopping amplitude  $|t_2|$  for  $N_s = 320$ . For small  $|t_2|$ , the characteristic level structure is not yet formed. Only when  $|t_2|$  is around 0.15–0.2, in-gap states, which are clearly separated from the quasicontinuum, emerge close to the valence band edge. A similar finite-size effect is also observed in the spectrum for fixed  $|t_2| = 0.2$  but variable system size  $N_s$  (see Fig. 9). For the smallest size with  $N_s = 80$ , the in-gap levels are not yet well separated from the rest of the states. However, they emerge for larger systems.

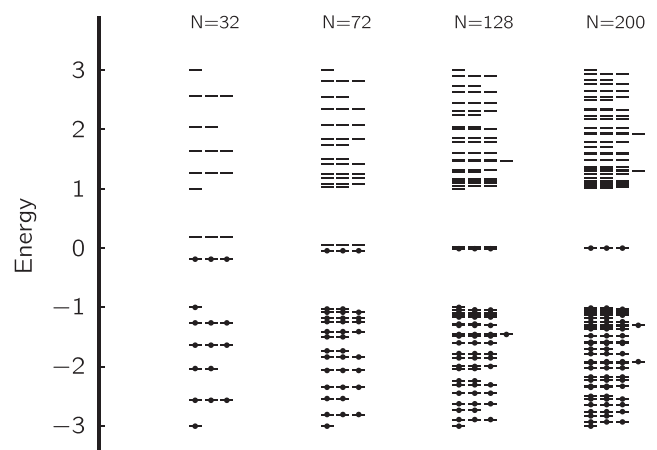


FIG. 7. Energy levels for octahedron as a function of system size (32 sites to 200 sites). Occupied levels are indicated with a black dot, assuming that exactly half of all states (bulk and corner) are occupied. Parameters of the model are  $t_1 = 1.0$ ,  $|t_2| = 0.2$ , and  $\phi = \pi/2$ .

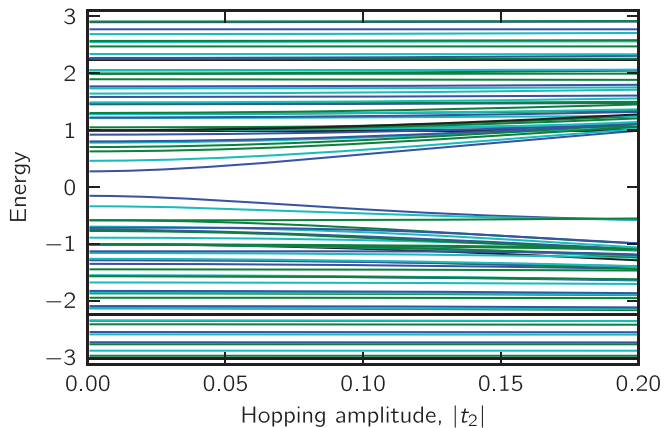


FIG. 8. (Color online) Eigenvalues of the icosahedron model as a function of the second-neighbor hopping parameter amplitude  $|t_2|$ . In-gap states close to the valence band edge appear when  $|t_2|$  is about 0.15 – 0.2. Phase of the second-neighbor hopping parameter is  $\phi = \pi/2$ ,  $t = 1$ , and  $N_s = 320$ . Nondegenerate levels are colored black, twofold-degenerate states red, threefold-degenerate states green, and fourfold-degenerate states blue.

### 3. Tetrahedral nanosurfaces

Eventually, we also discuss the finite-size effects for the tetrahedral systems where they appear to be strongest. Figure 10 shows the dependence of the spectrum on  $|t_2|$  for  $N_s = 324$ . We find that a sizable second-neighbor hopping amplitude of  $|t_2| \sim 0.2$  is required to identify in-gap levels appearing close to the conduction band. Figure 11 shows the spectrum for various system sizes at fixed  $|t_2| = 0.2$ . Only for the largest system with  $N_s = 100$  the corner states are more or less well separated from the quasicontinuum of the remaining states.

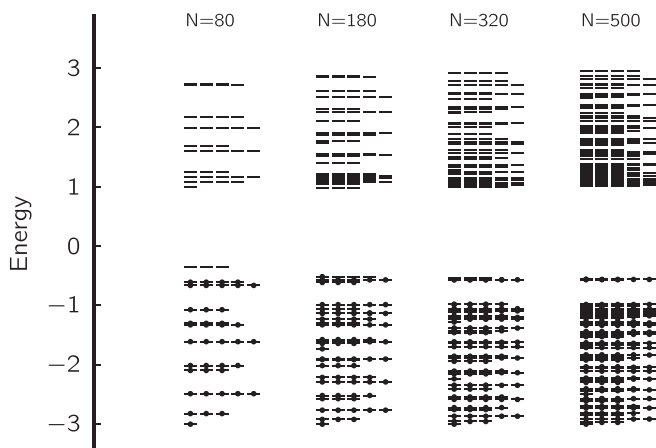


FIG. 9. Energy levels for the icosahedron as a function of system size (80 to 500 sites). Occupied levels are indicated with a black dot, assuming that exactly half of all states (bulk and corner) are occupied. Parameters of the model are  $t_1 = 1.0$ ,  $|t_2| = 0.2$ , and  $\phi = \pi/2$ .

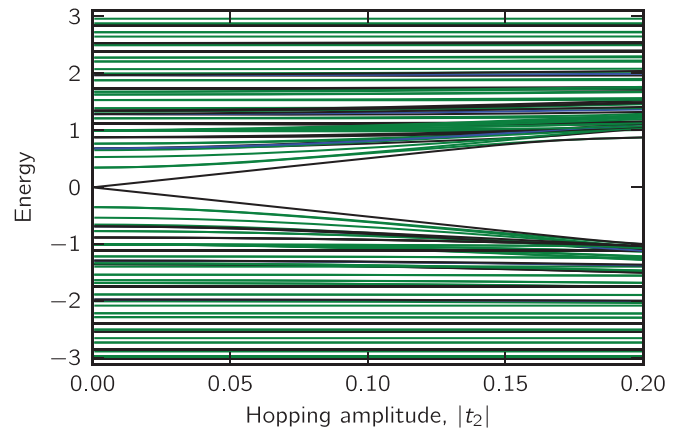


FIG. 10. (Color online) Eigenvalues of the tetrahedron model as a function of the second-neighbor hopping parameter amplitude  $|t_2|$ . In-gap states close to the conduction band edge appear for  $|t_2| \approx 0.2$ . Phase of the second-neighbor hopping parameter is  $\phi = \pi/2$ ,  $t = 1$ , and  $N_s = 324$ . Nondegenerate levels are colored black, twofold-degenerate states red, threefold-degenerate states green, and fourfold-degenerate states blue.

## V. SPLITTING OF CORNER LEVELS

### A. Overview

The tight-binding calculations presented in the previous section (Sec. II) demonstrated that if the bulk Hamiltonian is in the Chern-insulator phase, the electronic spectra of sufficiently large polyhedral nanosurfaces contain in-gap states which are clearly separated from the quasicontinuum of the remaining states. Furthermore, the number of in-gap states equals the number of corners of the polyhedron. However, because of the coupling between the corner states, the degeneracy is lifted in a characteristic way, as summarized in Fig. 1. The goal of this section is to better understand this corner-level splitting. As will be discussed in the following, the splitting can be understood by assigning a fixed chirality to the corner states.

In Sec. VB, we first study a general tight-binding model for the corner states alone. We show that in order to obtain an

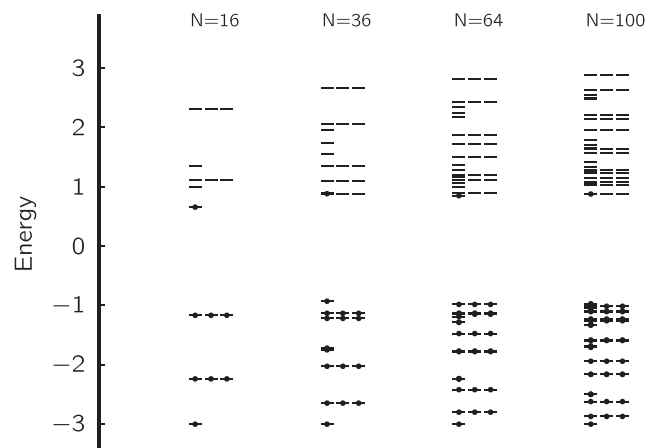


FIG. 11. Energy levels for the tetrahedron as a function of system size (16 to 100 sites). Occupied levels are indicated with a black dot, assuming that exactly half of all states (bulk and corner) are occupied. Parameters of the model are  $t_1 = 1.0$ ,  $|t_2| = 0.2$ , and  $\phi = \pi/2$ .

energy spectrum which is consistent with the observed lifting of the degeneracy, two magnetic monopoles have to be placed inside the polyhedron.

In Sec. V C, we relate this observation to the fact that the corner states are eigenstates of the  $n$ -fold rotation operator about an axis piercing the defect core. The angular momentum of these states is given by the Chern number  $C$ . We then argue that this leads to a nontrivial Berry phase contribution which can be represented by magnetic monopoles inside the polyhedra.

### B. Effective model for corner states

To study the splitting of the energy levels of the corner states, we first introduce a phenomenological model. The model focuses on the nearest-neighbor hopping processes between the corner states of the different Platonic solids studied in this work:

$$\mathcal{H}_{\text{corner}} = \sum_{\langle i,j \rangle} (t_{ij}^{\text{eff}} f_i^\dagger f_j + \text{H.c.}). \quad (13)$$

Here, the sum runs over nearest-neighbor pairs and the operator  $f_i^\dagger$  creates a corner state at the corner  $i$ . The hopping amplitude between corner  $i$  and  $j$  is given by  $t_{ij}^{\text{eff}}$ . It turns out that in order to reproduce the observed level splitting, it is crucial to allow for the possibility that the faces of the polyhedra are threaded by a magnetic flux. Therefore, we assume complex hopping amplitudes:

$$t_{ij}^{\text{eff}} = |t_{\text{eff}}| e^{i a_{ij}}. \quad (14)$$

The total phase accumulated when hopping around a triangle with corners  $i$ ,  $j$ , and  $k$  (labeled in a right-handed way) is then related to the flux through the triangle  $\phi_{ijk}$  by

$$a_{ij} + a_{jk} + a_{ki} = 2\pi \frac{\phi_{ijk}}{\phi_0}, \quad (15)$$

where, as before,  $\phi_0$  is the quantum of flux. By symmetry, we expect that the flux through each triangle is identical. This requires a configuration with an integer number of magnetic monopole quanta inside the solid. To model this situation, we consider flux lines which enter the solid through one face and then uniformly exit through the remaining faces, as illustrated in Fig. 12(a) for the case of the tetrahedron.

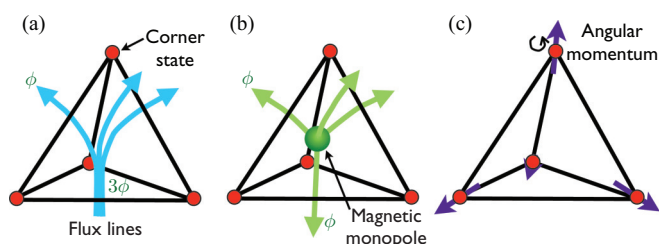


FIG. 12. (Color online) Illustration of different corner-state models (here shown for the tetrahedron). (a) Tight-binding model describing hopping between corner states in the presence of an external magnetic flux. (b) If the fluxes through each triangle are equal modulo  $\phi_0$ , an equivalent representation with a magnetic monopole in the center of the polyhedron exists. (c) In the absence of external fluxes, electrons can pick up the same complex phase from a Berry phase term arising due to an internal angular momentum.

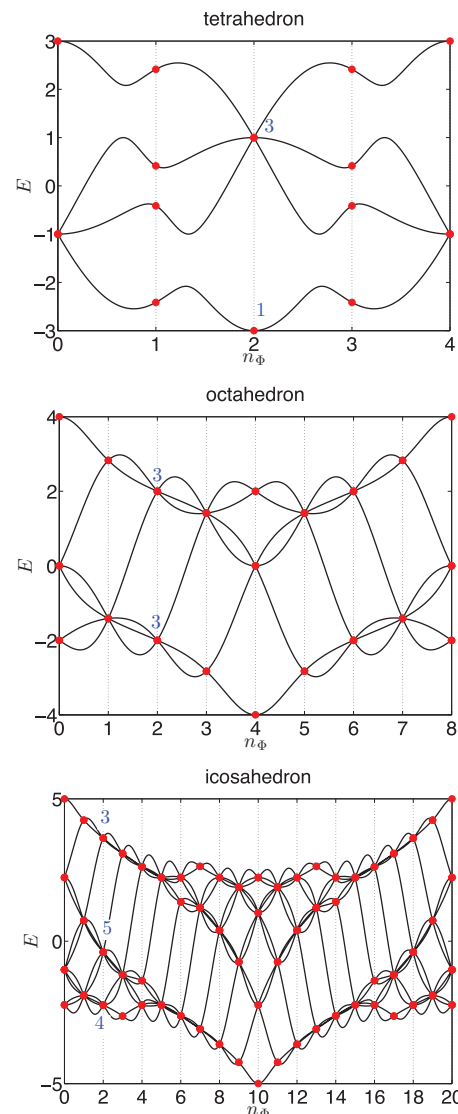


FIG. 13. (Color online) The energy spectrum of the corner tight-binding model on the tetrahedron, octahedron and icosahedron as a function of the number  $n_\phi$  of inserted magnetic monopoles (see main text). The degeneracies for  $n_\phi = 2$  are indicated in the plots.

Whenever the incoming flux is opposite equal to the outgoing flux through one of the faces modulo  $\phi_0$ , such a flux line configuration is indistinguishable from a magnetic monopole in the center of the solid as shown in Fig. 12(b). This condition is only satisfied if the flux through a single face is given by

$$\phi_{ijk} = n_\phi \frac{\phi_0}{F} \bmod \phi_0, \quad (16)$$

where  $n_\phi$  is an integer and  $F$  denotes the number of faces. Equation (16) is just Dirac's quantization condition for magnetic monopoles.

The energy spectra of the model (13) as a function of the number  $n_\phi$  of elementary magnetic monopoles inserted into the platonic solids are shown in Fig. 13. As described above, for noninteger values of  $n_\phi$ , the flux configuration does not correspond to Fig. 12(b) but to 12(a) with an outward pointing

flux  $\phi$  given by Eq. (16). Clearly, without a magnetic monopole ( $n_\phi = 0$ ), the splitting and degeneracies are not consistent with the numerical results of the full model shown in Fig. 4. Instead, a closer inspection shows that the splitting for  $n_\phi = 2$  is consistent for all the polyhedra, i.e.,  $1 + 3$  for the tetrahedron,  $3 + 3$  for the octahedron, and  $4 + 5 + 3$  for the icosahedron.

The  $n_\phi = 2$  magnetic monopole, which has to be placed inside the solids to reproduce the observed energy splitting, should not be confused with the fictitious flux  $\phi_f$  given in Eq. (5) (and which was also considered in the continuum approximation to spherical fullerenes<sup>15,52</sup>). The fictitious flux  $\phi_f$  produces the corner states in the first place, while the  $n_\phi = 2$  monopole is required to properly describe the coupling between the corner states.

### C. Chiral corner states

What is the reason for the occurrence of the  $n_\phi = 2$  monopole? In the following, we argue that this is a result of the chiral nature of the corner states. Indeed, the analysis of the continuum model for an isolated disclination<sup>33</sup> shows that the defect states carry a finite angular momentum  $J_z = C = \pm 1$  with respect to the  $n$ -fold rotation axes through the center of the  $n$ -gonal defect. On the polyhedral surfaces, the symmetry axis of the  $C_n$  rotations point outward through the corners of the polyhedron. Consequently, when the electrons hop from corner to corner, the quantization axes changes as well. As a result, if the electron hops around the triangle with corners  $i$ ,  $j$ , and  $k$ , it picks up a nontrivial Berry phase given by

$$\phi_{ijk} = \Omega(\mathbf{e}_i, \mathbf{e}_j, \mathbf{e}_k) \sim \mathbf{e}_i \cdot (\mathbf{e}_j \times \mathbf{e}_k), \quad (17)$$

where  $\Omega(\mathbf{e}_i, \mathbf{e}_j, \mathbf{e}_k)$  is the solid angle subtended by the three unit vectors pointing from the center of the polyhedron to the three corners  $i$ ,  $j$ , and  $k$ . This Berry phase can be represented by a magnetic monopole with  $n_\phi = 2$  [see Fig. 12(c)]. Note that similar Berry phase contributions appear if an electron propagates in the background of magnetic moments with noncoplanar order.<sup>53</sup> We present more details in the Appendix.

## VI. CONCLUSIONS

In summary, we have studied Haldane's honeycomb lattice model on spherical nanosurfaces, namely, the tetrahedron, the octahedron, and the icosahedron. For parameters which correspond to the Chern-insulator phase in the infinite planar model, we found that each corner of the polyhedron carries a nontrivial bound state and we dubbed such molecules *topological fullerenes*. In the energy spectrum, the corner states show up as characteristic in-gap levels which are clearly separated from the quasicontinuum of the remaining levels. We related the occurrence of the corner states to the existence of nontrivial defect states bound to isolated wedge disclinations and discussed the lifting of the degeneracies within an effective model for the corner states. The presented example demonstrates that a two-dimensional nontrivial bulk invariant can manifest itself in the energy spectrum of a *closed* surface with no boundaries. While our findings are based on the study of the Haldane model, we speculate that similar results can be obtained in other models with odd Chern number,

such as the planar  $p$ -orbital model<sup>54</sup> or a twisted version of Haldane's model.<sup>55</sup> We also expect that our findings can be generalized to models with time-reversal symmetry but nontrivial  $\mathbb{Z}_2$  invariant, such as the Kane-Mele model.<sup>3,4</sup> In this case, the in-gap modes would consist of Kramer's doublets and the bound states can exhibit the phenomena of spin-charge separation.<sup>56-58</sup>

We now briefly comment on possible experimental realizations of time-reversal-invariant topological fullerenes. The first approach is based on endohedral carbon fullerenes.<sup>59</sup> Following the proposal to decorate graphene with  $5d$  adatoms to induce a large spin-orbit coupling,<sup>21</sup> we suggest that the icosahedron model could be realized by instead enclosing  $5d$  transition-metal ions within the sphere of the fullerenes. For the planar system, a nontrivial  $\mathbb{Z}_2$  invariant has been predicted (time-reversal symmetry is preserved).<sup>21</sup> We therefore speculate that such a nontrivial bulk  $\mathbb{Z}_2$  invariant would give rise to nontrivial corner states. Using the estimate  $\Delta_{SO} = 3\sqrt{3}|t_2| = 200$  meV for the spin-orbit induced gap<sup>21</sup> and the value  $t = 2.7$  eV for the nearest-neighbor hopping in graphene yields a ratio  $t_2/t \approx 0.02$ . Relating this rough estimate to the findings of Sec. IV C shows that in order to overcome the finite-size effect, molecules should consist of several hundred atoms. A second approach to topological fullerenes would be the use of different materials with large intrinsic spin-orbit coupling such as 2D bismuth or 2D tin. Owing to the buckled nature of the honeycomb lattice realized in these systems,<sup>22,24</sup> it is conceivable that these materials would prefer to form octahedral nanosurface (for which it is possible to globally define two sublattices). According to our calculations, finite-size effects are less pronounced for the octahedral nanosurfaces and the corner states more likely to be observed.

## ACKNOWLEDGMENTS

A.R. acknowledges collaboration on related projects with C. Lin and F. de Juan and financial support from the Swiss National Science Foundation. S.C. acknowledges discussion with D. Vanderbilt and support by the Director, Office of Energy Research, Office of Basic Energy Sciences, Materials Sciences and Engineering Division, of the U. S. Department of Energy under Contract No. DE-AC02-05CH11231 which provided for the tight-binding calculations. J.E.M. acknowledges financial support from NSF DMR-206515.

## APPENDIX: CONTINUUM DESCRIPTION

### 1. Rotations and wedge disclinations

The (planar) Haldane model (3) for  $\Delta = 0$  possesses a sixfold rotation symmetry about the center of a hexagon. In the following, we review how this symmetry is implemented in the effective low-energy description given by the following Dirac Hamiltonian:

$$H_D = -iv(\tau_z\sigma_x\partial_x + \sigma_y\partial_y) + m\tau_z\sigma_z. \quad (A1)$$

The Hamiltonian (A1) acts on a four-component spinor  $\Psi = (\psi_A, \psi_B, \psi_{A'}, \psi_{B'})$ ,  $\vec{\sigma} = (\sigma_x, \sigma_y, \sigma_z)$  are the Pauli matrices for the sublattices ( $A$ - $B$ ), and  $\vec{\tau} = (\tau_x, \tau_y, \tau_z)$  for the valley ( $K$ - $K'$ )

degree of freedom. The mass term  $m$  arises from a finite  $t_2$  in the topologically nontrivial phase.

Because the Dirac equation (A1) is the low-energy limit of a lattice model, spatial symmetries are realized differently than for fundamental Dirac fermions.<sup>60</sup> Indeed, translations and rotations need to account for the finite lattice constant through the valley quantum number. In particular, one can identify two contributions to the rotation operator of physical rotations by an angle  $\alpha$  around the center of a hexagon:<sup>30,60</sup>

$$R(\alpha) = R_{\text{lattice}}(\alpha)R_{\text{Dirac}}(\alpha). \quad (\text{A2})$$

Note that in the low-energy limit of Eq. (A1), a continuous rotation symmetry emerges

$$R(\alpha)^\dagger H_D R(\alpha) = H_D \quad (\text{A3})$$

with arbitrary  $\alpha$ . However, the restriction  $\alpha = f\pi/3$  with  $f$  integer holds for physical rotations. Before providing the explicit form of  $R(\alpha)$ , it is convenient to introduce a symmetry-adapted basis with two new sets of Pauli matrices<sup>61</sup>

$$\vec{\Sigma} = (\Sigma_x, \Sigma_y, \Sigma_z) = (\sigma_x \tau_z, \sigma_y, \sigma_z \tau_z), \quad (\text{A4})$$

$$\vec{\Lambda} = (\Lambda_x, \Lambda_y, \Lambda_z) = (\sigma_y \tau_x, \tau_z, -\sigma_y \tau_y). \quad (\text{A5})$$

$\vec{\Sigma}$  denotes the (pseudo)spin- $\frac{1}{2}$  degree of freedom arising from the sublattice structure and  $\vec{\Lambda}$  are the generators of SU(2) rotations in valley space. In this basis, the Hamiltonian (A1) in Fourier space is simply

$$H_D = v_F(\Sigma_x k_x + \Sigma_y k_y) + m \Sigma_z \quad (\text{A6})$$

and  $[\vec{\Lambda}, H_D] = 0$ .

We now provide the explicit form of  $R(\alpha)$ . The first contribution in Eq. (A2) is the well-known rotation operator for fundamental Dirac spinors

$$R_{\text{Dirac}}(\alpha) = e^{i\frac{\alpha}{2}(\Sigma_z + 2L_z)}, \quad (\text{A7})$$

where  $L_z = -i(x\partial_y - y\partial_x)$  is the  $z$  component of the orbital angular momentum and  $\Sigma_z = \sigma_z \tau_z$  the  $z$  component of the spin- $\frac{1}{2}$  degree of freedom (associated here with the  $A$ - $B$  sublattices). Hence, the generator for  $R_{\text{Dirac}}$  is the sum of spin and orbital momentum. Note that  $R_{\text{Dirac}}(2\pi)\Psi = -\Psi$  which would make the wave function double valued when rotated by  $2\pi$ . The second contribution in Eq. (A2),

$$R_{\text{lattice}}(\alpha) = e^{i\frac{3\alpha}{2}\Lambda_z}, \quad (\text{A8})$$

arises from the underlying lattice theory and compensates this minus sign. Indeed,  $R_{\text{lattice}}(2\pi)\Psi = -\Psi$ , so that the spinor is single valued under physical  $2\pi$  rotations  $R(2\pi)\Psi = \Psi$ . The reason for the existence of  $R_{\text{lattice}}$  is the fact that the Dirac cones are located at finite lattice momenta  $K$  and  $K'$ . It essentially accounts for the exchange of the valley and sublattice degrees of freedom when a rotation by  $\alpha = \pi/3$  is performed.

This analysis motivates us to define the total angular momentum as

$$\vec{J} = \vec{L} + \frac{1}{2}\vec{\Sigma} + \frac{3}{2}\vec{\Lambda}. \quad (\text{A9})$$

Because  $[J_z, H_D] = 0$ , we can choose an eigenbasis of  $H_D$  which simultaneously diagonalizes  $J_z$ .<sup>30,33</sup> In this basis, rotation by an angle  $\alpha = f\pi/3$  acts as

$$R(f\pi/3)\Psi(r, \phi) = (\tau i)^f \Psi(r, \phi + f\pi/3), \quad (\text{A10})$$

where  $(r, \phi)$  are polar coordinates and  $\tau = \pm 1$  denotes the chirality of  $\Psi$ :

$$\Lambda_z \Psi(r, \phi) = \tau \Psi(r, \phi). \quad (\text{A11})$$

According to Eq. (A10), for a wedge disclination, connecting the wave function across the seam requires a nontrivial boundary condition: the factor  $(\tau i)^f$  precisely yields the fictitious flux Eq. (5).

## 2. Chiral defect states and Berry phase

The solution of the continuum model in the presence of a disclination<sup>33</sup> shows that the bound state satisfies

$$\Lambda_z \Psi_0 = -(2L_z + \Sigma_z)\Psi_0 = \text{sign}(C)\Psi_0. \quad (\text{A12})$$

Thus, the defect states are eigenstates of  $J_z$  with eigenvalues  $j_z = \text{sign}(C)$ .

On a polyhedral surface, the quantization axis points outward through the corners of the polyhedron. When hopping from corner to corner, the quantization axis has to be adjusted which results in a nontrivial Berry phase. To calculate the Berry phase contribution, we note first that for an isolated disclination, the azimuthal part of the bound state with  $j_z = 1$  is simply  $e^{i\varphi} \sim |p_x\rangle + i|p_y\rangle$ . Next, we consider the surface of the sphere and ask what is the overlap between two defect states which are infinitesimally close to each other. We choose the spherical coordinates such that the defect states have the same altitude  $\theta$  on the sphere but are separated along the  $e_\phi$  direction by an infinitesimal amount  $\Delta\phi$ . In spherical coordinates, the first orbital is

$$|\psi^{(1)}\rangle = \frac{1}{\sqrt{2}}[|p_1(\theta, \phi)\rangle + i|p_2(\theta, \phi)\rangle]. \quad (\text{A13})$$

The second orbital is separated by  $\Delta\phi$  in the direction  $e_\phi$  from the first orbital and is given by

$$\begin{aligned} |\psi^{(2)}\rangle &= \frac{1}{\sqrt{2}}[|p_1(\theta, \phi + \Delta\phi)\rangle + i|p_2(\theta, \phi + \Delta\phi)\rangle] \\ &= (1 - i \cos \theta \Delta\phi)|\psi^{(1)}\rangle - \frac{i}{\sqrt{2}} \sin \theta \Delta\phi |p_3(\theta, \phi)\rangle. \end{aligned} \quad (\text{A14})$$

The effective hopping amplitude between the two states can now be obtained from the overlap

$$t_{\Delta\phi}^{\text{eff}} = -t \langle \psi^{(1)} | \psi^{(2)} \rangle = -t(1 - i \cos \theta \Delta\phi) = -t e^{i a_\phi \Delta\phi},$$

where the Berry connection is identified as  $a_\phi(\theta, \phi) = -\cos \theta$ . Integrating along a closed path from  $\phi = 0$  to  $2\pi$  yields a Berry flux

$$\Phi_B = -2\pi \cos \theta \pmod{2\pi}. \quad (\text{A15})$$

Hence, the Berry flux is identified with the solid angle enclosed by the path of the electron on the sphere. For the hopping between the corners of the polyhedron, this result implies that each triangular face is pierced by a flux

$$\Phi_F = 4\pi/F. \quad (\text{A16})$$

This is precisely Eq. (16) with  $n_\phi = 2$  ( $\hbar = 1$ ).

- <sup>1</sup>F. D. M. Haldane, *Phys. Rev. Lett.* **61**, 2015 (1988).
- <sup>2</sup>C.-Z. Chang, J. Zhang, X. Feng, J. Shen, Z. Zhang, M. Guo, K. Li, Y. Ou, P. Wei, L.-L. Wang, Z.-Q. Ji, Y. Feng, S. Ji, X. Chen, J. Jia, X. Dai, Z. Fang, S.-C. Zhang, K. He, Y. Wang, L. Lu, X.-C. Ma, and Q.-K. Xue, *Science* **340**, 167 (2013).
- <sup>3</sup>C. L. Kane and E. J. Mele, *Phys. Rev. Lett.* **95**, 226801 (2005).
- <sup>4</sup>C. L. Kane and E. J. Mele, *Phys. Rev. Lett.* **95**, 146802 (2005).
- <sup>5</sup>B. A. Bernevig and S.-C. Zhang, *Phys. Rev. Lett.* **96**, 106802 (2006).
- <sup>6</sup>B. A. Bernevig, T. L. Hughes, and S.-C. Zhang, *Science* **314**, 1757 (2006).
- <sup>7</sup>M. König, S. Wiedmann, C. Brune, A. Roth, H. Buhmann, L. W. Molenkamp, X.-L. Qi, and S.-C. Zhang, *Science* **318**, 766 (2007).
- <sup>8</sup>F. D. M. Haldane, *Phys. Rev. Lett.* **74**, 2090 (1995).
- <sup>9</sup>C. Xu and J. E. Moore, *Phys. Rev. B* **73**, 045322 (2006).
- <sup>10</sup>C. Wu, B. A. Bernevig, and S.-C. Zhang, *Phys. Rev. Lett.* **96**, 106401 (2006).
- <sup>11</sup>M. Dresselhaus, G. Dresselhaus, and P. Eklund, *Science of Fullerenes and Carbon Nanotubes* (Academic, New York, 1996).
- <sup>12</sup>A. Kitaev, *AIP Conf. Proc.* **1134**, 22 (2009).
- <sup>13</sup>S. Ryu, A. P. Schnyder, A. Furusaki, and A. W. W. Ludwig, *New J. Phys.* **12**, 065010 (2010).
- <sup>14</sup>A. M. Essin, J. E. Moore, and D. Vanderbilt, *Phys. Rev. Lett.* **102**, 146805 (2009).
- <sup>15</sup>J. González, F. Guinea, and M. A. H. Vozmediano, *Nucl. Phys. B* **406**, 771 (1993).
- <sup>16</sup>D. Kolesnikov and V. Osipov, *Phys. Part. Nuclei* **40**, 502 (2009).
- <sup>17</sup>D. Golberg, Y. Bando, O. Stéphan, and K. Kurashima, *Appl. Phys. Lett.* **73**, 2441 (1998).
- <sup>18</sup>P. A. Parilla, A. C. Dillon, B. A. Parkinson, K. M. Jones, J. Alleman, G. Riker, D. S. Ginley, and M. J. Heben, *J. Phys. Chem. B* **108**, 6197 (2004).
- <sup>19</sup>Q. H. Wang, K. Kalantar-Zadeh, A. Kis, J. N. Coleman, and M. S. Strano, *Nat. Nanotechnol.* **7**, 699 (2012).
- <sup>20</sup>C. Weeks, J. Hu, J. Alicea, M. Franz, and R. Wu, *Phys. Rev. X* **1**, 021001 (2011).
- <sup>21</sup>J. Hu, J. Alicea, R. Wu, and M. Franz, *Phys. Rev. Lett.* **109**, 266801 (2012).
- <sup>22</sup>S. Murakami, *Phys. Rev. Lett.* **97**, 236805 (2006).
- <sup>23</sup>C.-C. Liu, W. Feng, and Y. Yao, *Phys. Rev. Lett.* **107**, 076802 (2011).
- <sup>24</sup>Y. Xu, B. Yan, H.-J. Zhang, J. Wang, G. Xu, P. Tang, W. Duan, and S.-C. Zhang, *Phys. Rev. Lett.* **111**, 136804 (2013).
- <sup>25</sup>C. Sabater, D. Gosálbez-Martínez, J. Fernández-Rossier, J. G. Rodrigo, C. Untiedt, and J. J. Palacios, *Phys. Rev. Lett.* **110**, 176802 (2013).
- <sup>26</sup>An even number of defects with opposite  $f$  is also possible on the torus, for example, two pentagon and two heptagon defects.
- <sup>27</sup>R. Bianco and R. Resta, *Phys. Rev. B* **84**, 241106 (2011).
- <sup>28</sup>P. M. Chaikin and T. C. Lubensky, *Principles of Condensed Matter Physics* (Cambridge University Press, Cambridge, UK, 2000).
- <sup>29</sup>P. E. Lammert and V. H. Crespi, *Phys. Rev. Lett.* **85**, 5190 (2000).
- <sup>30</sup>P. E. Lammert and V. H. Crespi, *Phys. Rev. B* **69**, 035406 (2004).
- <sup>31</sup>A. Roy and M. Stone, *J. Phys. A: Math. Theor.* **43**, 015203 (2010).
- <sup>32</sup>S. N. Naess, A. Elgsaeter, G. Helgesen, and K. D. Knudsen, *Sci. Technol. Adv. Mater.* **10**, 065002 (2009).
- <sup>33</sup>A. Rüegg and C. Lin, *Phys. Rev. Lett.* **110**, 046401 (2013).
- <sup>34</sup>Y. Ran, Y. Zhang, and A. Vishwanath, *Nat. Phys.* **5**, 298 (2009).
- <sup>35</sup>Y. Ran, arXiv:1006.5454.
- <sup>36</sup>V. Juričić, A. Mesaros, R.-J. Slager, and J. Zaanen, *Phys. Rev. Lett.* **108**, 106403 (2012).
- <sup>37</sup>R.-J. Slager, A. Mesaros, V. Juricic, and J. Zaanen, *Nat. Phys.* **9**, 98 (2013).
- <sup>38</sup>N. Read and D. Green, *Phys. Rev. B* **61**, 10267 (2000).
- <sup>39</sup>W. P. Su, J. R. Schrieffer, and A. J. Heeger, *Phys. Rev. Lett.* **42**, 1698 (1979).
- <sup>40</sup>C.-Y. Hou, C. Chamon, and C. Mudry, *Phys. Rev. Lett.* **98**, 186809 (2007).
- <sup>41</sup>A. Rüegg and G. A. Fiete, *Phys. Rev. B* **83**, 165118 (2011).
- <sup>42</sup>J. He, Y.-X. Zhu, Y.-J. Wu, L.-F. Liu, Y. Liang, and S.-P. Kou, *Phys. Rev. B* **87**, 075126 (2013).
- <sup>43</sup>J. C. Y. Teo and T. L. Hughes, *Phys. Rev. Lett.* **111**, 047006 (2013).
- <sup>44</sup>S. Gopalakrishnan, J. C. Y. Teo, and T. L. Hughes, *Phys. Rev. Lett.* **111**, 025304 (2013).
- <sup>45</sup>A. P. Schnyder, S. Ryu, A. Furusaki, and A. W. W. Ludwig, *Phys. Rev. B* **78**, 195125 (2008).
- <sup>46</sup>J. C. Y. Teo and C. L. Kane, *Phys. Rev. B* **82**, 115120 (2010).
- <sup>47</sup>D. Zheng, G.-M. Zhang, and C. Wu, *Phys. Rev. B* **84**, 205121 (2011).
- <sup>48</sup>C. Fang, M. J. Gilbert, and B. A. Bernevig, *Phys. Rev. B* **86**, 115112 (2012).
- <sup>49</sup>C. Fang, M. J. Gilbert, and B. A. Bernevig, *Phys. Rev. B* **87**, 035119 (2013).
- <sup>50</sup>J. Jung, Z. Qiao, Q. Niu, and A. H. MacDonald, *Nano Lett.* **12**, 2936 (2012).
- <sup>51</sup>M. Zarenia, O. Leenaerts, B. Partoens, and F. M. Peeters, *Phys. Rev. B* **86**, 085451 (2012).
- <sup>52</sup>J. González, F. Guinea, and M. A. H. Vozmediano, *Phys. Rev. Lett.* **69**, 172 (1992).
- <sup>53</sup>K. Ohgushi, S. Murakami, and N. Nagaosa, *Phys. Rev. B* **62**, R6065 (2000).
- <sup>54</sup>M. Zhang, H.-h. Hung, C. Zhang, and C. Wu, *Phys. Rev. A* **83**, 023615 (2011).
- <sup>55</sup>E. Alba, X. Fernandez-Gonzalvo, J. Mur-Petit, J. K. Pachos, and J. J. Garcia-Ripoll, *Phys. Rev. Lett.* **107**, 235301 (2011).
- <sup>56</sup>Y. Ran, A. Vishwanath, and D.-H. Lee, *Phys. Rev. Lett.* **101**, 086801 (2008).
- <sup>57</sup>X.-L. Qi and S.-C. Zhang, *Phys. Rev. Lett.* **101**, 086802 (2008).
- <sup>58</sup>F. F. Assaad, M. Bercx, and M. Hohenadler, *Phys. Rev. X* **3**, 011015 (2013).
- <sup>59</sup>L. Dunsch and Y. Shangfeng, *Electrochem. Soc. Interface* **15**, 34 (2006).
- <sup>60</sup>A. Mesaros, D. Sadri, and J. Zaanen, *Phys. Rev. B* **82**, 073405 (2010).
- <sup>61</sup>F. de Juan, *Phys. Rev. B* **87**, 125419 (2013).